PCCP

Accepted Manuscript

ROYAL SOCIETY OF CHEMISTRY

www.rsc.org/pccp

Zinc oxide as defect-dominated material in thin films for photovoltaic applications – experimental determination of defect levels, quantification of composition, and construction of band diagram

Maciej Krzywiecki*[,1,2], Lucyna Grządziel[2], Adnan Sarfraz[1], Danish Iqbal[1], Anna Szwajca[3], Andreas Erbe[1]

[1] Max-Planck-Institut für Eisenforschung GmbH, Max-Planck-Str. 1, 40237 Düsseldorf, Germany
[2] Institute of Physics – CSE, Silesian University of Technology, Konarskiego 22B, 44-100 Gliwice, Poland.
[3] Faculty of Chemistry, A. Mickiewicz University, Umultowska 89b, 61-614 Poznań, Poland

Abstract

In present work, thin ZnO layers were synthesized by the sol-gel method with subsequent spin-coating on Si (100). We show that the detailed analysis of lab-recorded photoemission spectra and combination with Kelvin probe data yielded work function, ionization energy, valence band – Fermi level separation and hence enabled construction of band diagrams of the examined layers. With small modifications in preparation, very different films can be obtained. One set shows a homogeneous depth-dependent n carrier distribution, another a significant carrier concentration gradient from n type of conductivity to almost metal-like n^+ character. Likewise, the surface morphology can be tuned from a uniform, compact surface with spherical single-nm sized grain-like features, to a structured surface with 5-10 nm tall crystallites with (002) dominating crystal orientation.

Basing on the band-bending and the energy levels observed, defects of contradictory nature, i.e. acceptor-donor-trap (ADT) properties were identified. These defects may be groups of point defects, with opposite character. The ADT states affect the energy levels of the oxide layers and due to their nature cannot be considered in photoemission experiment mutually independent.

The versatile nature of the synthesis provides us with the opportunity to tune the properties with a high degree of freedom, at low processing costs, yielding layers with exotic electronic structure. Such layers are interesting candidates for applications in photovoltaic and nanoelectronic devices.

Keywords:

Transparent conducting oxides, zinc oxide, thin films, spin-coat, sol-gel, XPS, UPS, energy structure, scanning probe microscopy

---

* Corresponding author, tel.: +48 (32) 237 20 01; fax: +48 (32) 237 22 16

E-Mail: Maciej.Krzywiecki@polsl.pl (M. Krzywiecki)

Content

1. Introduction

ZnO is a wide-gap semiconductor with optical transparency in the visible range. The optical and electronic properties of ZnO thin films resulted in applications in electronic and optoelectronic devices such as transparent conductors [1,2,3], solar cell windows [4,5,6], ultraviolet lasers [7], gas sensors [8,9], refractive index sensors [10], light emitting diodes [11,12], and surface acoustic wave devices [13]. As n-type semiconductor, ZnO layers could be also a good candidate for dye-synthesized solar cells [14] or for use in hybrid inorganic-organic electronic devices [15,16].

Due to the vast range of applications, numerous ZnO film preparation techniques have been employed, such as chemical vapor deposition [17,18], ion beam deposition [19], molecular beam epitaxy [20], magnetron sputtering [21,22,23], atomic layer deposition [24] or laser pulse deposition [25]. All mentioned methods resulted with well-established ZnO films with structure and properties more or less tuned to desired application. However, the disadvantage of these methods is that they require advanced expensive setups.

Alternatives include electrochemical growth [26], or corrosion processes [27]. Another relatively cheap method is based on a sol-gel process. Particularly studies of colloidal ZnO nanocrystals are extensively performed last times in terms of the crystallite size and luminescence-controllable synthesis [28,29]. Only few works have been recently devoted to the optical and structural characterization of the sol-gel derived ZnO thin films. In most cases the sol-gel technique is followed by another uncomplicated process which is spin-coat deposition [30,31,32]. Authors focused on the growth conditions influence on the on the physical properties of ZnO thin films. Hence, a number of questions arose together with the expansion of knowledge on this topic. The electronic structure considerations or problems of ambipolar doping are discussed only in chosen works (e.g. [11,12]). Nevertheless the zinc oxide thin film energy structure still remains not fully revealed. Especially for photovoltaic applications, the mutual influence of the morphology and chemical composition on the electronic properties is crucial. For instance, understanding the role of native point defects (like vacancies) or the nature of impurities is a milestone on the way to control the properties (e.g. conductivity) of ZnO layers [33]. By controlling the properties of the material one can easily tune the performance of the device under development; hence deeper understanding of the ZnO internal structure is essential [34].

In present work we focus on the comprehensive characterization of ZnO layers, obtained by a sol-gel technique, designed for bulk heterojunctions inorganic-organic exciton solar cells. The intended application requires a surface morphology that in combination with phthalocyanine-based organic semiconductors, ZnO layer should create a bulk heterojunction. According to our last studies on copper and iron phthalocyanine [35,36], the surface should be moderately developed for such applications, with roughness in the range of few nm in such a manner that the incoming organic molecules could easily penetrate the outer ZnO surface creating bulk interdigital-like structure. Because of the exciton mean free path (which is ranging dependently on material from ~7 nm up to ~30 nm [37]), the overall thickness of such created p-n junction should not exceed 15-30 nm.

The main aim of this work is to use laboratory-based photoemission techniques to construct a band diagram of ZnO sol-gel layers. Furthermore, information on the morphology is required, which is obtained by scanning probe and scanning electron microscopy.

2. Experimental details

2.1 Sample preparation

Silicon (100) wafers (SiMat) (n-type, P-doped, 5-10 Ω·cm) were used as substrates. Wafers were cleaned in an ultrasonic bath by sequentially soaking them in acetone, isopropanol, and de-ionized water for 15 min per cycle. Then, wafers were blown with nitrogen and dried in a furnace in 110°C for 30 min.

ZnO sol was synthesized by dissolving zinc acetate in ethylene glycol at 0.5 M. The solution was stirred and heated to 70°C. Then, ethanolamine (MEA) was added drop-wise. The sol was further stirred at 70°C for 30 min and left for aging for 12 h. All reagents were purchased from VWR and used as received.

Spin-coat deposition (spin-coater P6700, Specialty Coating Systems Inc.) was done in cycles. Spinning was conducted at 500 rpm for 2 s, 2000 rpm for 1 s and 6000 rpm for 29 s. Before spinning, the solution was covering the entire substrate surface. After deposition the samples were dried in air for 10 min at 110°C. After the desired number of cycles, samples were annealed in a tube furnace at 350°C for 4 h in ambient atmosphere.

Within this work, we report experiments conducted with samples after four deposition cycles (denoted as "4c"), and samples after a single cycle (denoted as "1c").

2.2 Experimental techniques

Surface topography was investigated by atomic force microscopy (AFM) and scanning electron microscopy (SEM). Non-contact mode AFM investigations were done on a VEECO Nanoscope IV using Al-coated Olympus OMCL-AC160TS-R3 tips (resonant frequency 300 kHz, force constant 2.1 N/m). AFM data were quantified using Gwyddion. The images were leveled and filtered. Quantitative analysis used Gwyddion built-in algorithms [38].

SEM images were taken with a Carl Zeiss LEO 1550 VP microscope combined with an in-lens detector (working distance 3 mm, ETH voltage 10 kV). For elemental analysis and basic chemical characterization of the sample, energy-dispersive X-ray spectroscopy (EDX; Oxford Instruments) was applied, with a setup integrated into the SEM.

X-ray diffraction (XRD) was conducted using a Bruker-AXS D8 with Cu-Kα source.

Surface chemical composition was examined with X-ray photoemission spectroscopy (XPS), combined with an Ar^+ ion etching steps for depth profiling on a Physical Electronics PHI Quantera II spectrometer equipped with an Al-K_α micro-focused (with quartz crystal monochromator) source with the photon energy 1486.74 eV and dual-beam charge neutralizer. The pass energy was set to 140 eV for the survey spectra (energy step 0.2 eV) and 26 eV for recording the individual core levels spectra (energy step 0.05 eV). The XPS system base pressure was $2 \cdot 10^{-8}$ Pa. All XPS spectra were recorded at a take-off angle of 45°.

The etching rate (spot size 2 µm x 2 µm; U= 1 kV) was kept at 3.7 nm/min. The binding energy was calibrated to Au4$f_{7/2}$ (84.0 eV) [39].

XPS data were analysed by curve fitting using CASA XPS software. Each peak was represented by a sum of Gaussian (70%) and Lorentzian (30%) lines, while the secondary electron background was subtracted utilizing the Shirley function. Where necessary, peaks were resolved with spin-orbit multiplets. The full width at half maximum (FWHM) of the same components was allowed to vary within a narrow range. We used the lowest possible number of components to fit the data satisfactory, i.e. to obtain acceptably low residual values. The estimated uncertainty for particular

component position determination in XPS measurements was within 0.05 eV. Quantitative analysis, including component ratio determination, was done with use of CASA XPS embedded relative sensitivity factors (RSF) and algorithms.

Ultraviolet photoemission spectroscopy (UPS) measurements were done using the SPECS PHOIBOS 150 analyzer. Excitation was performed by the 21.22 eV He I line of a He discharge lamp. He I β and He I γ satellites were numerically subtracted from the recorded spectra [40]. The estimated uncertainty was 0.05 eV for the obtained work function and 0.07 eV for the ionization energy.

Spectroscopic ellipsometry was used to estimate the deposited zinc oxide thicknesses. Measurements were conducted using a Sentech Instruments SE 800 spectroscopic ellipsometer working in the wavelength range 350 nm–810 nm (1.55–3.55 eV) at angles of incidence from 55° – 70° in 5° steps. Analysis was performed with the instrument's software, using a Si substrate/Si oxide/ZnO oxide/air multilayer Cauchy model with parameters implemented in the software. Silicon oxide thickness was determined before deposition of ZnO as 2.5 nm.

Surface potential scans were performed on a commercial scanning Kelvin probe (SKP) system (Wicinski – Wicinski GbR, Wuppertal, Germany) with a 100 µm NiCr tip in a dry nitrogen atmosphere. Before experiments, the probe potential was calibrated against a $Cu/CuSO_4$ reference and against Au plates.

3. Results and discussion

3.1 Surface topography and structure

Before proceeding to a detailed electronic structure determination of the ZnO films, the films where characterized by a number of analytical techniques.

Ellipsometric determination of the layer thickness yields values of ~22 nm (1c) ~29 nm (4c). Increasing the number of deposition cycles hence increases only slightly the thickness, due to dissolution of the previously deposited sol before annealing.

AFM measurements (Fig. 1) of the annealed ZnO layers show the surface with uniformly distributed small spherical grains. The estimated RMS surface roughness is 1.4 nm (1c) and 2.8 nm (4c), hence it increases with increasing film thickness. The roughness of the Si wafer substrate was <0.4 nm. Fig. 1 clearly exhibits that an increase in the number of deposition cycles is accompanied by an increase in the grain diameter. Control experiment conducted for silicon substrates revealed the RMS roughness below 0.25 nm; hence it shouldn't have impact on the layers' topography.

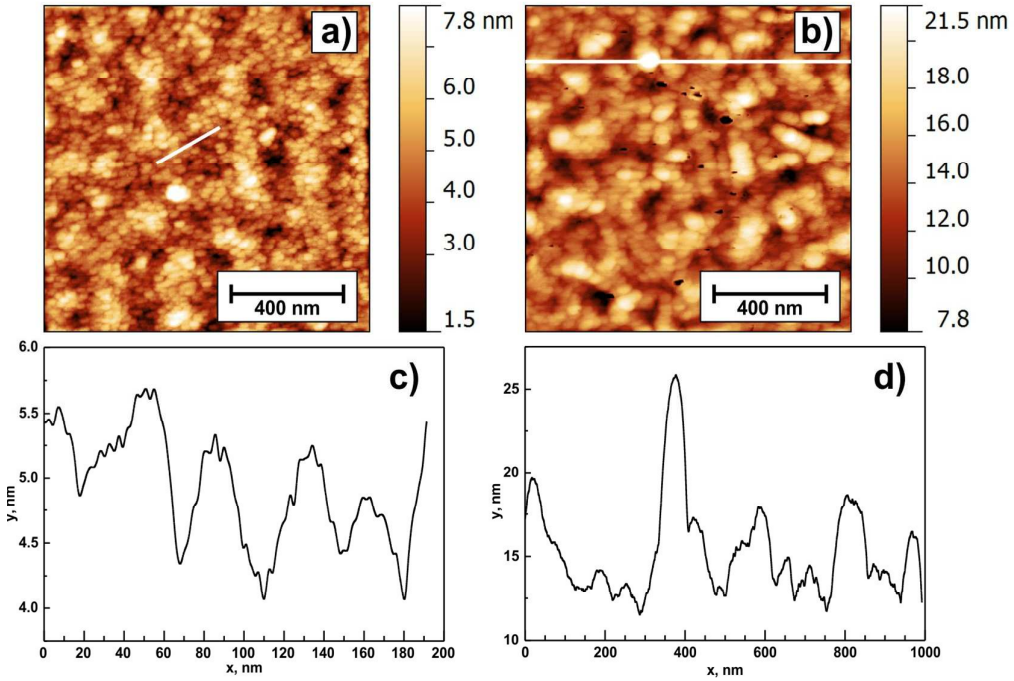

Fig. 1 AFM 1 µm x 1 µm height images obtained for samples 1c (a) and 4c (b). Panels (c) and (d) show the extracted profiles marked with white lines in the corresponding images.

The estimated grain diameter determined from profiles is 25-30 nm for sample 1c and 50-75 nm for sample 4c (Fig. 1 c and d, respectively). An interesting feature present in the 4c ZnO layer is uniformly distributed "column-like" crystallites protruding from the sample surface. Their height is estimated as 10-15 nm. Such protruding crystallites are not visible for thinner samples. The grain coarsening with increasing number of deposition cycles is confirmed by SEM images shown in Fig. 2.

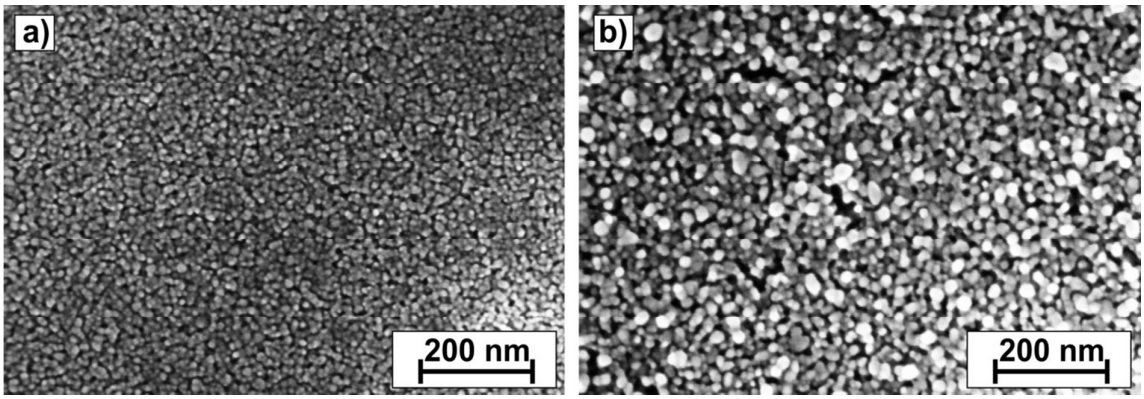

Fig. 2 SEM images of samples 1c (a) and 4c (b).

The SEM images also confirm existence of "column-like" crystallites in case of 4c samples, and the more homogenous surface with uniform crystallite distribution in case of 1c sample. The "column-like" structure is a direct consequence of the partial dissolution of the previously deposited sol layer for multiple deposition cycles.

XRD measurements (Fig. 3) show two strong reflections at 56.2° and at 34.5°. The first one can be attributed to some amorphous compounds that did not convert to crystalline ZnO or to (311) base silicon substrate [41] while the latter is the reflection originating from ZnO (002) crystallites [42].

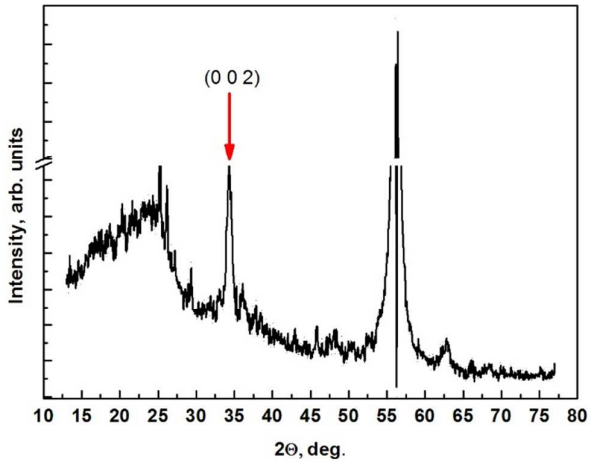

Fig. 3 XRD pattern of 4c sample. Peak at about 56° is a peak present also in reference measurements.

The Scherrer's formula [43]

$$L = \frac{K_s \lambda}{\beta' cos\theta} \quad (1)$$

was used for estimation of the volume mean crystallite size. In above formula, L is the mean crystallite diameter, K_s a shape-dependent constant (considered as close to unity, here K_s = 0.9 [42]), λ the X-ray wavelength (0.154 nm), β' – the full width at half maximum (FWHM) of the peak under consideration (in radians) and ϑ the corresponding Bragg angle. The estimated volume crystallite size in case of the layers is ranging from 10 nm for sample 1c to 15 nm for sample 4c. In agreement with microscopic experiments, the crystallite size is larger for the sample with higher number of deposition cycles. Actual numbers derived from XRD are lower compared to AFM, because of the different averaging.

As a result, application of several sol deposition cycles leads to roughening of the surface because of an increase in individual grain size, at a moderate increase in layer thickness. As the same time, a modification of the overall morphology is observed.

3.2 Photoemission studies

3.2.1 Chemical composition analysis

Application of XPS stepwise ion etching allowed for the determination of surface and depth-dependent chemical composition of examined ZnO layers. Fig. 4 shows survey spectra taken for several chosen steps of ion etching. ZnO-related energy regions are well visible, i.e. Zn (2p, 3s, 3p, 3d), Zn LMM and O1s. Carbon contamination can be monitored in the C1s region. With increasing depth, the substrate peaks (Si2p and Si2s) are becoming more pronounced, while those originating from ZnO are diminishing. The XPS spectral line assignment was based on LaSurface [44] database.

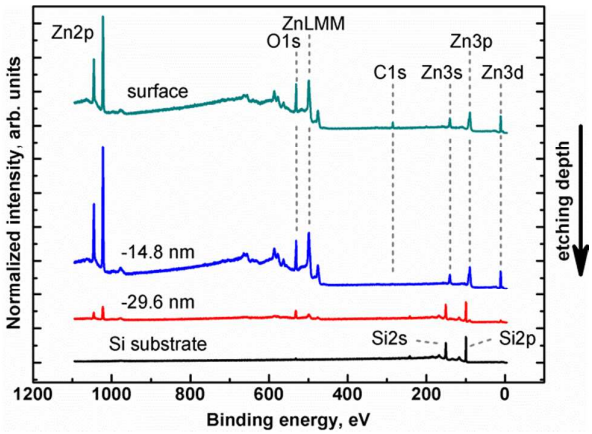

Fig. 4 Survey spectra obtained for as deposited 4c sample (surface) and three chosen steps of ion etching. All characteristic XPS regions are clearly visible.

Carbon could be present in the samples as residual from the preparation, or as a surface contamination. C1s energy region analysis (not shown) revealed that over 90% of carbon contamination is present at the sample's surface. In the interior of the film only trace amounts of carbon are detectable. This indicates that the prolonged annealing process is sufficient to remove residual solvent from the film. Also substrate surface carbon contamination doesn't play significant role as checked in substrate XPS control measurement before ZnO layer deposition.

The chemical state of the examined oxide layer is examined in two ways. First, the Auger α–parameter is evaluated and analyzed [45]. Secondly, standard main oxygen (O1s) and zinc (Zn2p) regions are analyzed quantitatively. The evaluation of the Auger α–parameter involves a method in which the differences in bonding negativity according to Pauling theory [46] is calculated. The chemical state of examined species is determined from the energy difference between a representative XPS peak and a suitable Auger peak. The Auger parameter α is defined as [47]:

$$\alpha = E_k(jkl) + E_B(i) \quad (2)$$

where $E_K(jkl)$ is the is the kinetic energy of the Auger transition *jkl* and $E_B(i)$ is the binding energy of an electron in atomic level *i.* In our case, the Zn $2p_{3/2}$ and Zn LMM should be considered. A lower α indicates a lower electron density at the atom, i.e. a higher oxidation state. Fig. 5 shows the α–parameter of 4c sample determined for different ion etching depths. The inset presents example of Zn LMM Auger peak for non-etched 4c sample's surface.

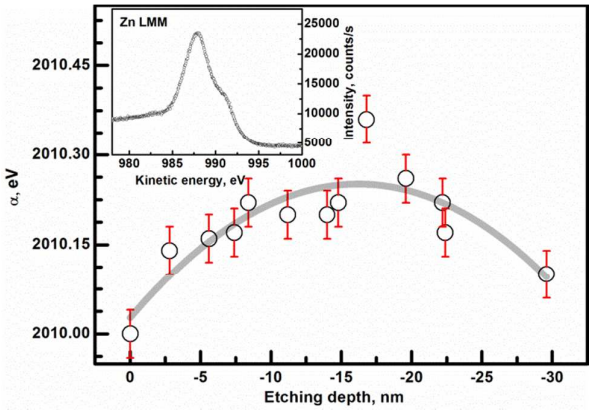

Fig. 5 Determined α–parameter as function of ion etching depth for 4c sample. The depth dependence was fitted with a polynomial to show the trend in the data. Inset shows the Auger Zn LMM energy region.

The general trend of the data is marked by fitted polynomial line. It is easy to see that there are significant differences between surface layer and film. A higher oxidation state near the surface is expected, as the surface is in contact with the ambient atmosphere in the annealing and also prior to XPS measurements. A decrease of the α–parameter is also detected near the ZnO / substrate interface. This decrease may originate from the influence of the substrate oxide film [48]. More details can be obtained from an analysis of the O 1s and Zn 2p regions.

Fig. 6 a presents the O 1s intensity as a function of etching depth. The overall peak consists of at least three components, from which only two are detectable at one time. The inset of Fig. 6a shows two components of the O1s peak recorded for 4c sample etched to ~16.8 nm. Two layer-related components at ~531 eV and ~532.5 eV are well visible in the spectra and can be attributed respectively to oxygen – metal (here: Zn-O) bonding and probably oxygen on a split-interstitial configuration [49] or oxide near Zn vacancies. The third component (~532 eV) appears after ~30 nm of ion etching and hence originates from the substrate oxide. The initial increase in O 1s signal after the first etching cycle is attributed to the removal of carbon contamination from the sample surface.

Quantification of the Zn 2p region allowed the determination of Zn/O concentration ratio, which is shown in Fig. 6 b.

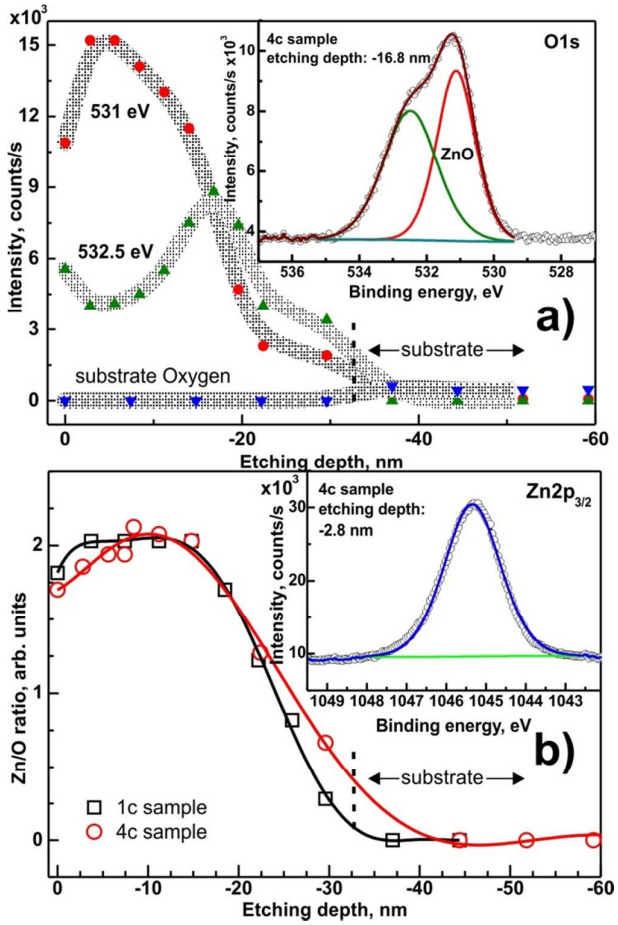

Fig. 6 a) Components of O 1s XPS region as function of depth of ion etching for 4c sample. Inset: Decomposition of O 1s peak recorded for 16.8 nm etched sample. Grey lines are eye-guiding spline connections. b) Zn/O ratio as function of depth of ion etching for samples 1c and 4c. Inset: Zn $2p_{3/2}$ XPS peak. Lines between points are polynomial fits.

The data presented in Fig. 6 b for sample 4c shows that the Zn/O ratio is increasing from the value of 1.7 up to 2.1 (estimation uncertainty 0.06) at ~10 nm in depth, then it stabilizes till ~18 nm and then it decreases monotonically until the ZnO / substrate interface. For the 1c sample, the Zn/O ratio starts ~1.80 at the surface, and slightly increases to ~2.00 for a depth of less than 3 nm. It remains stable till ~14 nm and monotonically decreases similar to the 4c sample.

The difference in the Zn/O ratio can be attributed to more pronounced surface oxidation during annealing process after deposition in case of 4c samples, because 4c samples exhibit a more developed surface topography in comparison to densely packed crystallites in 1c samples. The more "open" structure of 4c samples favors oxygen uptake from the atmosphere. A second contribution may be the partial dissolution of the previously deposited layer when applying several layers consecutively, thus resulting in a gradient of the Zn concentration. The decrease of the Zn/O towards the substrate is caused by substrate contributions and an overall decrease of O 1s and Zn 2p intensity.

Overall, an atomic Zn/O ratio of ~2 is obtained in the center of the film, which is far from the expected value of 1 for stoichiometric ZnO. This observed difference can only be explained by defects, and will be discussed in Section 3.2.2.

3.2.2 Electronic structure of the ZnO films

Detailed analysis of the valence band and Zn 3d energy region (0-15 eV binding energy) of the XP spectra and additional application of UPS allowed for the description of the ZnO electronic properties. Because ion etching depth profile was done only for XPS, the UPS information should be treated here as a starting point for relating exactly XPS energies to the Fermi level. XPS and UPS have different depth of information, because of different photoelectron escape depths for different excitation energies. According to the Seah-Dench diagram [50], while the UPS yields a photoemission signal from few nanometers, the XPS is giving information down till 10 nm. Hence, different surface and layer's interior species contribute differently to the overall signal.

Considering Fermi level for the analyzer and investigated sample are equal, one can determine the energy difference between Fermi level and the valence band onset E_F-E_V, the work function φ, and ionization energy Φ. Fig. 7 a and b presents the magnification of the high energy cut-off and low energy onset of the UPS spectrum taken for samples 1c and 4c. The intercept of the background line with a linear approximation of high energy cut-off taken between 1/3 and 2/3 of the cut-off's maximum intensity allows the determination of the surface work function of examined samples according to [51]

$$\varphi = h\nu - E_{cut-off} \quad (3)$$

where *hν* is the excitation energy (here 21.22 eV) and $E_{cut\text{-}off}$ is the interception point. The obtained work function values were φ=3.32 eV and φ=3.18 eV (uncertainty 0.05 eV) for samples 1c and 4c, respectively. Next, the ionization energy was determined as [51]

$$\Phi = \varphi + (E_F - E_V) \quad (4)$$

where E_F-E_V is the energy difference between valence band onset and Fermi level position (Fig. 7 b). The values for E_F-E_V were determined as 3.05 eV and 2.85 eV for samples 1c and 4c, respectively. Hence, the ionization energy is equal to 6.37 eV for 1c and 6.07 eV (uncertainty 0.07 eV) for 4c sample.

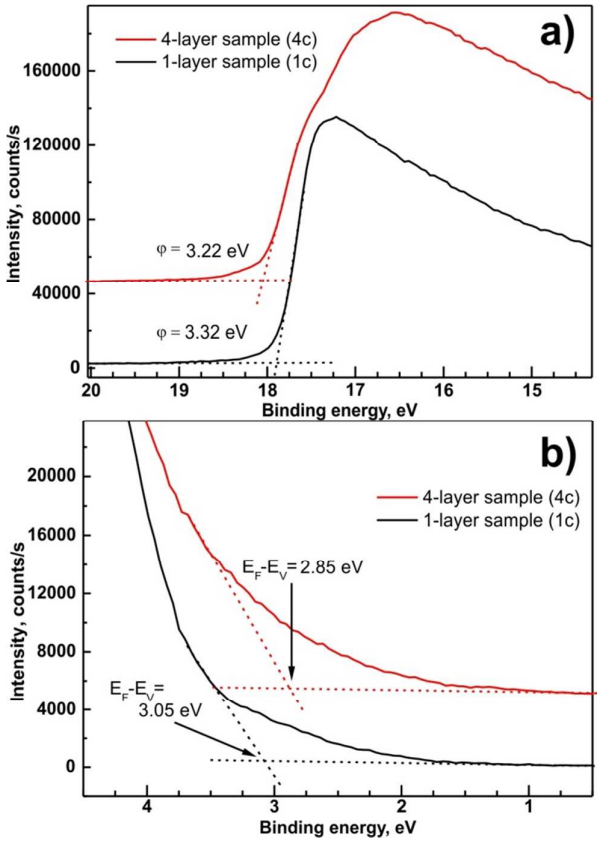

Fig. 7 High energy cut-off (a) and valence band onset (b) of UPS spectra recorded for samples 1c and 4c.

The values of the work function are considerably smaller than the 3.74 eV obtained on layers grown by radio frequency magnetron sputter deposition [52]. On the other hand, our values are quite consistent with the values obtained for (0 0 0 1) ZnO Zn-terminated surfaces annealed at 700 K [53].

With this input from the UPS data, the depth dependent XPS measurements from the valence band region were analyzed. E_F-E_V values were determined from examined samples as a function of layer thickness. Simultaneously, the Zn 3d peak position was analyzed.

Fig. 8 presents high-resolution valence band spectra taken for sample 4c for different etching depths. The Zn 3d XPS peak is well visible as well as the valence band onset. The region of energies between 6-8 eV corresponds to O 2p, C 2p and Si 3s levels and due to their surface sensitivity in XPS method are not considered for further analysis. A binding energy of 0 corresponds to the Fermi level position. It can be clearly seen in the spectra that the onset of photoemission consists of more than one component. For a direct quantification, the band needs to be decomposed. In the presented spectra, three distinct contributions can be observed (marked as I, II and III in Fig. 8). Component (II) is detectable up to an etching depth of 15 nm and is attributed to defect-related energy levels in the band gap of zinc oxide layer. Component (III) is related to the substrate – induced distortions of the ZnO electronic structure.

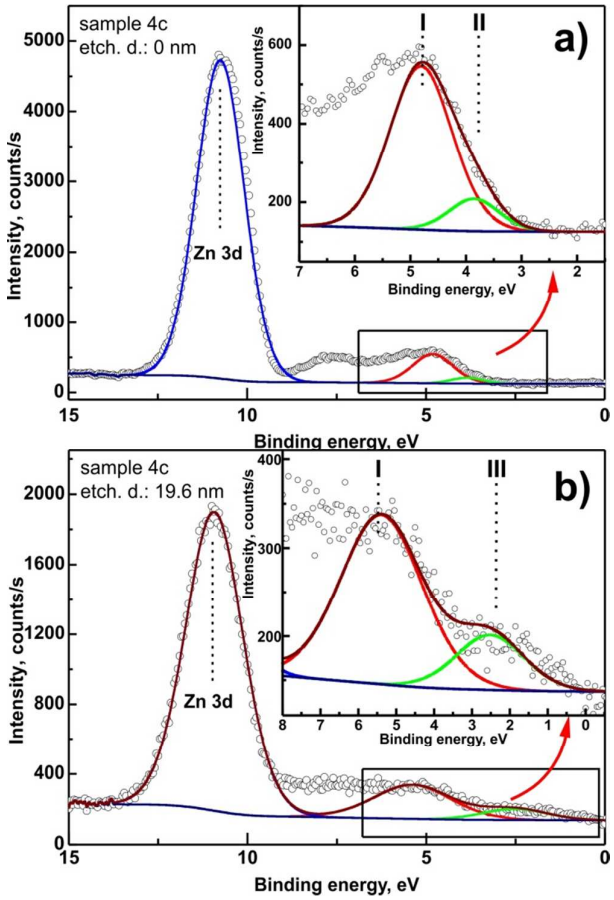

Fig. 8 Valence band region and Zn 3d XPS peaks recorded for before etching (a) and after etching 19.6 nm (b). Insets: Magnification of the valence band onset. Two components are distinguishable in each case. For component (I, II and III) description – see text.

Each of the components introduces distortions of the E_F-E_V energy difference. The E_F-E_V values as function of ion etching depth determined for the three components are presented in Fig. 9. Dependent on the depth that is probed by XPS, the mutual relation of the components affects the overall E_F-E_V energy difference. The synergy effect can be described using an equivalent component for the valance band representation. Hence we construct such component with the area equal to the sum of the particular components areas and position which is weighted mean of the respective positions (we use components I, II and III areas as weights). The onset of the equivalent component determines the resulting E_F-E_V energy distance (full black circles in Fig. 9)

The resulting E_F-E_V value is changing from 2.8 eV to 3.3 eV in the range of the first 18 nm from the samples surface. The component (II) contribution is detectable up to 15 nm from the surface, while component (III) is starts to appear in the spectra from 15 nm. The component (I) is present from the initial surface up to ~22 nm. At this depth, the resultant E_F-E_V value drops significantly to the value of 0.6 eV consistent with weakly doped n-type silicon substrate (in comparison to 0.56 eV for intrinsic Si [54]). The overall thickness obtained in this ion etching experiment is consistent with the thickness obtained from ellipsometry. The analogous analysis made for sample 1c shows an initial increase of E_F-E_V from 3.0 eV at the surface to 3.2 eV at the depth of ~4 nm (not shown in figure). Then the value stabilizes and drops rapidly down to the substrate–related value of 0.6 eV. The changes in electronic structure occur at similar depths as changes in the Zn/O ratio are observed (Fig. 6 b).

The inset of Fig. 9 shows the Zn 3d peak position as a function of depth. The changes, within the accuracy of the method, follow the valence band position changes with respect to Fermi level.

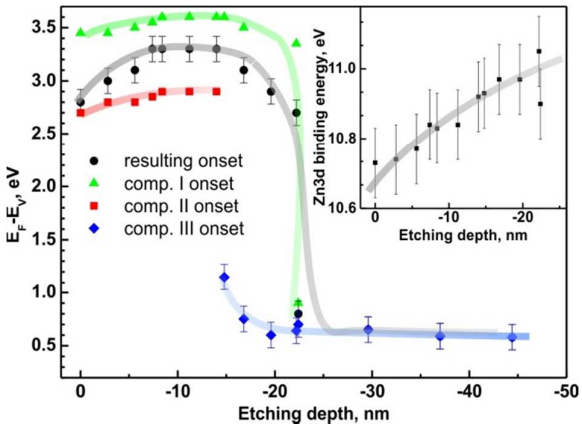

Fig. 9 E_F-E_V as function of ion etching depth (sample 4c). Inset: Zn 3d XPS peak position as function of depth of ion etching.

For a comprehensive description of the depth-dependent ZnO electronic structure, a determination of the vacuum level as a function of ion etching depth is necessary. For this purpose, SKP measurements were performed. Fig. 10 shows the change of the contact potential difference (CPD) between SKP tip and the 4c sample surface. The measurement was done on the crater etched by the Ar^+ ions during XPS ion etching depth profiling. The tip of the SKP was probing the edge of the crater from an intact layer towards silicon substrate. Although the obtained potential values are given with respect to a different reference than those obtained from the photoemission methods, , the voltage differences equal changes of the work function Δφ, i.e. the energy difference between the Fermi level E_F and the vacuum level E_{Vac}. For sample 4c, Δφ equals 0.20 eV with the trend following the E_v and Zn 3d changes. The observed difference shows a drop in the vacuum level which causes a lowering of the work function towards deeper regions in the ZnO layers. The same analysis made for sample 1c (not shown) revealed Δφ ~0.10 eV. The SKP analysis was followed by carrier concentration calculations. We determined the value of negative carrier concentration *n* in ZnO as [55]

$$n = N_c \cdot \left(\frac{E_F - E_c}{kT}\right) \quad (5)$$

where N_c is effective density of states in conduction band, for ZnO $N_c = 3.7 \cdot 10^{18}$ cm^{-3} [56], *k* is the Boltzmann constant and T the absolute temperature, here 300 K. The energetic distance E_F-E_c, is calculated as the difference between the ZnO band gap E_g = 3.37 eV [33] and the value of E_F-E_v received from XPS measurements of the valence band region.

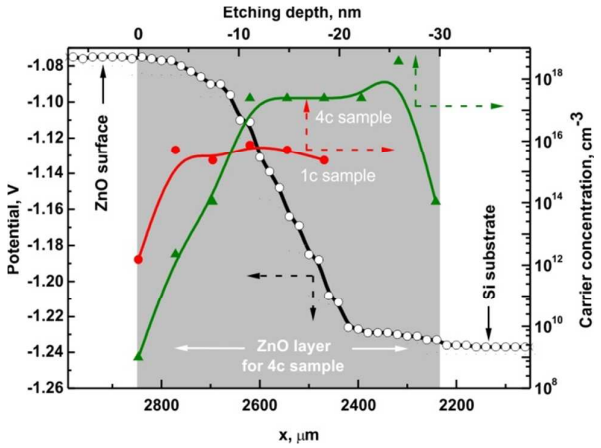

Fig. 10 SKP profile (empty circles – left-bottom scale) of sample 4c. The abscissa corresponds to the position on the edge of the ion etched crater in the ZnO layer. The ordinates represent the potential difference between tip and samples surface. Concentration of n-type charge carriers (right-top scale) is shown as a function of ion etching depth for samples 1c (full circles) and 4c (triangles). Dashed arrows additionally indicate the corresponding axis.

Fig. 10 shows depth-dependent carrier concentration for samples 1c (full circles) and 4c (triangles). The carrier concentration graph shows significant differences between samples 1c and 4c. In case of sample 1c, the carrier concentration is changing within the first 3-4 nm starting from the sample surface and then stabilizes at the level of 10^{16} cm^{-3}. The depths levels at which changes are observed agree with those in the Zn/O ratio plot (Fig. 6 b). Sample 4c exhibits a gradual carrier concentration change within the first 10 nm and then stabilizes at the level of 10^{18} cm^{-3}. The drop of the carrier concentration for the last point is due to layer/substrate interaction and discussed earlier as caused by signal overlap of the XPS signals used for calculating the numbers presented here. The data in Fig. 10 highlights the differences between samples 1c and 4c in chemical composition and electronic properties. It also clarifies the differences between regions near the surface and regions inside the thin film for both samples.

All data determined above were gathered and utilized to construct a band-like energy structure diagram of spin-coated ZnO layers which is shown in Fig. 11. The diagram was drawn for sample 4c, because the depth–dependent chemical and energy changes are not so pronounced in case of thinner, more uniform and compact sample 1c. Analyzing the energy levels in the ZnO layer, three different regions can be distinguished. They are named, starting from surface side moving towards substrate, as n, n^{+}, and oxide/substrate interface. The naming of the first two regions originates from different electronic properties describing zinc oxide in that particular region.

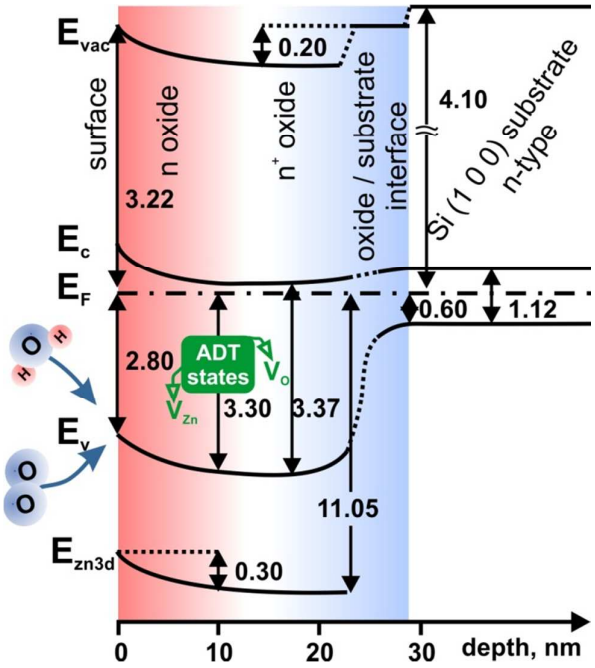

Fig. 11 Band-like diagram of electronic structure of deposited ZnO layers for sample 4c. Si work function from [57], Si band gap from [58]. The work function change at the oxide/substrate interface can be interpreted as interface dipole effect [59]. Acceptor-Donor-Trap states alter the energy levels.

Starting from the surface, the n region extends 10 nm deep into the ZnO layer. Within this region, the energy levels are altered, which is manifested by the significant (~0.5 eV) band bending of the valence and conduction bands in comparison to next region denoted as n^+. The Zn 3d core level is following this trend. With the band bending, the work function is decreasing by 0.2 eV.

Within the n region, there is a considerable variation of the Zn/O ratio from 1.7 to 2.1, as oxygen uptake occurs from the surface towards the interior of the ZnO layer. Oxygen from the ambient atmosphere may be incorporated into the layer from the surface region (n) during annealing. Alternatively, water vapor may adsorb after annealing. The defects introduce additional states in the band gap below the Fermi level, which alter the valence band position and consequently E_F-E_V. They also improve stoichiometry at the samples surface reducing the Zn/O ratio.

The n^+ region is characterized by a significantly higher carrier concentration and the relatively small separation between Fermi level E_F and bottom of the conduction band E_C. In this region, the ZnO tends towards metal-like electronic structure. The origin of this variation is most likely the increase of oxygen vacancy concentration towards the interior region of the zinc oxide film.

Looking at the direction of the band bending, one expects charge carrier depletion in the n region. Recalling the results shown in Fig. 10 one can see that excess carrier concentration is considerably lower in the n than n^+ region.

However it has to be remembered that the photoemission signal, which is the main basis of constructed diagram comes from so called XPS information depth, which can be up to 10 nm. In this terms the different energetic states has their contribution to the overall photoemission signal. It means that the states decreasing the carrier concentration (states rather close to surface) and states increasing carrier concentration (more distant from surface and bulk – related) are simultaneously observed in photoemission spectra giving combined effect [60]. The states are characterized by different intensity. Consequently, the states which are present in the ZnO spectrum must have a competing nature [61]. On the one hand, the states should be donor-type due to increased

accumulation in the n^+ region, while on the other hand lowering the number of excess carriers in n region suggests existence of states with acceptor-like or trap nature.

A possible explanation for this situation is considering a pairing of oxygen and zinc vacancies (V_O and V_{Zn} respectively). Although the layer is strongly oxygen deficient throughout, with oxygen deficiency is increasing towards the layer interior, the competing zinc vacancies are introducing the acceptor states. Simultaneously, due to existence of V_O and V_{Zn} together, the native ZnO structure has to be significantly deformed. This deformation might introduce additional trap levels which alter the photoemission experiment, indirectly changing the carrier concentration distribution pattern. Hence, from the experimental point of view, at the surface, three different and mutually competing energy states are present as one group. Therefore, we propose to treat them as one group of acceptor-donor-trap states (referred to as "ADT" states).

The individual states of different nature were described with their energy levels [62]. As a result, Zn vacancies should be treated as deep acceptors with the three possible charge state configurations, V^{0}_{Zn}, V^{-}_{Zn} and V^{2-}_{Zn}. V_{Zn} having the lowest formation energy among the native point defects in ZnO; hence it is expected to be the dominant point defect class. Generally, the absence of a Zn atom in the ZnO lattice should leave four oxygen dangling bonds with six electrons. As stated in [33], dangling bonds can combine into double occupied symmetric states located deep in the valence band, and three almost degenerate states in the band gap close to the top of the valence band. In our situation, the latter states are the center of attention, because the states can easily accept two additional electrons (they are partially occupied by four electrons [33]) altering the electronic structure in the band gap. The ADT state donor part is connected with the oxygen vacancies. Such vacancies have, among the donor defects, the lowest formation energy [33]. This low formation energy is caused by the Madelung potential, which is the main driving force for the localization of electrons in the place normally occupied by the oxygen anion in the ZnO structure. The replacement of oxygen by two free electrons in the defected lattice minimizes the energetic cost of the vacancy formation [63]. Free electrons have been observed in ZnO experimentally by electron paramagnetic resonance [64]. States associated with these electrons should act as shallow donor [61,65,66]. On the other hand, density functional calculations [67] have shown that V_O cause very deep donor states which cannot contribute to n-type conductivity. This statement is not consistent with our results. However, because the neutral V_O is located ~1 eV below the bottom of the conduction band [30], it can compete with the acceptor states V_{Zn} nearby during photoexcitation of the sample affecting the photoemission experiment. Ionized vacancies like V^{+}_{O} are also deep donors [68,69], but according to the literature, V^{+}_{O} is not thermodynamically stable [70].

The state originating from the coordinatively unsaturated anion O^{2-} [71] may also be present as a donor state. Such anions may be introduced by though the environment, e.g. from O_2 or water vapor.

The last component of the ADT states that remains to be discussed are the traps located in the band gap of ZnO. Such electron traps affect significantly the results of the photoemission experiment, and consequently the calculation of free carriers. The most probable are shallow electron traps $ZnO_{corner}(e^-)$ at morphological features like surface inhomogeneity. The more structured surface with column-like features observed for sample 4c (Section 3.1) hints in this direction, as less traps are expected for samples 1c with the more uniform surface. Similar morphology-related trap states were observed earlier [72]. Moreover, electrons can be entrapped in a localized cavity center of a missing O atom either from the interior region or from the surface of the ZnO [33]. Hence, oxygen vacancies may be responsible for the observation of trap states.

4. Conclusions

The presented work shows preparation and characterization of extremely oxygen-deficient low-work function zinc oxide layers with a gradient of carrier concentration. Preparation uses an easy and cost-effective sol-gel process followed by spin-coating. Surface morphology can be tuned by the number of deposition cycles. Such layers can be applied in bulk heterojunction-based photovoltaic devices.

The sol/gel preparation technique permits control over the carrier concentration profile from subsurface region towards the interior film depending on particular needs. This work demonstrates two radically different films: one with significant carrier concentration gradient, and the other with a homogeneous carrier distribution.

The observed band bending, together with the information on the composition, leads to the conclusion that several types of defects combine their properties to a group with donor, acceptor and trap properties, which cannot be treated independently. The origins of such “acceptor-donor-trap” (ADT) states may be oxygen and zinc vacancies, morphology-induced trap states and surface states resulting from interaction with ambient atmosphere.

The sol/gel preparation technique offers still much wider opportunities for preparation than explored in this work. For instance, the column-like morphology observed for some films makes them candidates for applications in photovoltaic and nanoelectronic device preparation, e.g. in hybrid inorganic-organic electronic devices with p-type phthalocyanines. Addition of foreign components into the solution offers the opportunity to tune doping levels more precisely than shown here. While in gas phase processes, the variation of composition of a thin film is more straightforward to realize, the ease of solution techniques makes it worth wile to take up the challenge of unraveling the interplay between preparation and electronic properties of the resulting films. A result may be knowledge-based design with completely new properties in long-known materials.

5. Acknowledgments

This scientific work was partially supported by the Polish budget for science in years 2013-2015 (by Ministry for Science and Higher Education) within Iuventus Plus IP2012 019072 project through the Silesian University of Technology, Institute of Physics.

References

[1] J.B. Webb, D.F. Williams, M. Buchanan, Appl. Phys. Lett. 39 (1981) 640.
[2] M.J. Brett, R.W. McMahon, J. Affinito, R.R. Parsons, J. Vac. Sci. Technol. A 1 (1983) 352.
[3] H. S. Uhm, G. C. Kwon and E. H. Choi, Appl. Phys. Lett. 99 , 261502 (2011).
[4] Y. Hagiwara, T. Nakada, A. Kunioka, Sol. Energy Mater. Sol. Cells 67 (2001) 267.
[5] D. R. Kumar, D. Manoj and J. Santhanalakshmi, RSC Adv., 4 (2014) 8943.
[6] C. Battaglia, J. Escarré, K. Söderström, M. Charrière, M. Despeisse, F.-J. Haug & C. Ballif 2011 Nature Photon. 5, 535.
[7] Linhua Xu, Xiangyin Li, Yulin Chen, Fei Xu, Appl. Surf. Sci, 257 (2011) 4031.
[8] S.S. Badadhe, I.S. Mulla, Sens. Actuators B 143 (2009) 164.
[9] D. Zappa, E. Comini and G. Sberveglieri, 2013 Nanotechnology 24 444008.
[10] R. Moirangthem, A. Erbe, Appl. Phys. Lett. 103 (2013) 051108.
[11] M. Willander, O. Nur, N. Bano and K. Sultana, New J. Phys. 11 (2009) 125020.
[12] F.-L. Kuo, Y. Li, M.. Solomon, J. Du and N. D. Shepherd, 2012 J. Phys. D: Appl. Phys. 45 065301
[13] C.L. Jia, K.M.Wang, X.L. Wang, X.J. Zhang, F. Lu, Opt. Exp. 13 (2005) 5093.
[14] Z. H. Chen, C. P. Liu, H. E. Wang, Y. B. Tang, Z. T. Liu, W. J. Zhang, S. T. Lee, J. A. Zapien and I. Bello, 2011 J. Phys. D: Appl. Phys. 44 325108.
[15] C. Reese, M. Roberts, M.M. Ling, and Z. Bao, Mater. Today, 7 (2004) 20.
[16] A.L. Briseno, T.W. Holcombe, A.I. Boukai, E.C. Garnett, S.W. Shelton, J.J.M. Frechet, P. Yang, Nano Lett. 10 (2010) 334.
[17] Y. Natsume, H. Sakata, T. Hirayama, H. Yanagida, J. Appl. Phys. 72 (1992) 4203.
[18] M. Chandran, B. Tiwari, C.R. Kumaran, S.K. Samji, S.S. Bhattacharya and M.S. Ramachandra Rao, J. Phys. D: Appl. Phys. 45 (2012) 202001.
[19] T. Chen, S.-L. Liu, Q. Xie, C. Detavernier, R. L. Van Meirhaeghe, X.-P. Qu, J Mater Sci: Mater Electron 21 (2010) 88.
[20] M.A. Pietrzyk, M. Stachowicz, A. Wierzbicka, P. Dluzewski, D. Jarosz, E. Przeździecka, A. Kozanecki, J. Cryst. Growth, 408 (2014) 102.
[21] K.B. Sundaram, A. Khan, Thin Solid Films 295 (1997) 87.
[22] X. Jiang, F. L. Wong, M. K. Fung, and S. T. Lee, App. Phys. Lett. 83 (2003) 1875.
[23] C. Besleaga, G.E. Stan, A.C. Galca, L. Ion, S. Antohe, Appl. Surf. Sci. 258 (2012) 8819.
[24] D. Bekermann et al., Cryst. Growth Design 10, 2011-2018 (2010).
[25] K.L. Narasimhan, S.P. Pai, V.R. Palkar, R. Pinto, Thin Solid Films. 295 (1997) 104.
[26] Y. Chen, P. Schneider, B.-J. Liu, S. Borodin, B. Ren, A. Erbe, Phys. Chem. Chem. Phys. 15 (2013) 9812.
[27] D. Iqbal, A. Kostka, A. Bashir, A. Sarfraz, Y. Chen, A.D. Wieck, A. Erbe, ACS Appl. Mater. Interfaces, 6 (2014) 18728.
[28] X. Liu, M.T. Swihart, Nanoscale, 5 (2013) 8029.
[29] X. Tang, E.S. Guang Choo, L. Li, J. Ding and J. Xue, Chem. Mater. 22 (2010) 3383.
[30] Y. Natsume, H. Sakata, Thin Solid Films 372 (2000) 30.
[31] Linhua Xu, Xiangyin Li, Yulin Chen, Fei Xu, Appl. Surf. Sci. 257 (2011) 4031.
[32] A. H. Jayatissa, K. Guo, T. Gupta, A.C. Jayasuriya, J Mater Sci: Mater Electron, 20 (2009) 577.
[33] A. Janotti and C.G. Van de Walle, Rep. Prog. Phys. 72 (2009) 126501.
[34] A. Ney, M. Opel, T.C. Kaspar, V. Ney, S. Ye, K. Ollefs, T. Kammermeier, S. Bauer, K-W. Nielsen, S.T.B. Goennenwein, M.H. Engelhard, S. Zhou, K. Potzger, J. Simon, W. Mader, S.M. Heald, J.C. Cezar, F. Wilhelm, A. Rogalev, R. Gross, S.A. Chambers, New J. Phys. 12 (2010) 013020.
[35] M. Krzywiecki, L.Grządziel, J. Bodzenta, J. Szuber, Thin Solid Films, 520 (2012) 3965.
[36] M. Krzywiecki, L.Grządziel, J. Juszczyk, A. Kaźmierczak-Bałata, A. Erbe, J. Bodzenta, J. Phys. D.: Appl. Phys. 35 (2014) 335304.
[37] H.R. Kerp, H. Donker, R.B.M. Koehorst, T.J. Schaafsma, E.E. van Faassen, Chem. Phys. Lett. 298 (1998) 302.
[38]http://gwyddion.net/documentation/user-guide-en/
[39] I. Lindau, P. Pianetta, K.Y. Yu, W.E. Spicer, Phys. Rev. B, 16 (1976) 492.
[40] J. Blochwitz, T. Fritz, M. Pfeiffer, K. Leo, D.M. Alloway, P.A. Lee and N.R. Armstrong Org. Electron. 2 (2001) 97.
[41] M. Chandran, B. Tiwari, C. R. Kumaran, S. K. Samji, S.S. Bhattacharya and M. S. Ramachandra Rao, J. Phys. D: Appl. Phys. 45 (2012) 202001.

[42] R. Yogamalara, R. Srinivasan, A. Vinu, K. Ariga, A. C. Bose, Solid State Commun. 149 (2009) 1919.
[43] H.P. Klug & L.E. Alexander, X-Ray Diffraction Procedures, 2nd Ed., John Wiley & Sons Inc., 1974, p 687-703.
[44] www.lasurface.com/database/element.php
[45] M. Futsuhara, K. Yoshioka, O. Takai, Thin Solid Films 322 (1998) 274.
[46] L. Pauling, The Nature of the Chemical Bond, Chap. 3, Cornell University, Ithaca, NY, 1960.
[47] M. Futsuhara, K. Yoshioka, O. Takai, Thin Solid Films 322 (1998) 274.
[48] A.S. Komolov, S.N. Akhremtchik, E.F. Lazneva, Spectrochim. Acta A, 79 (2011) 708.
[49] P. Erhart, A. Klein, K. Albe, Phys. Rev. B 72 (2005) 085213.
[50] M.P. Seah, W.A. Dench, Surf. Interf. Anal. 1 (1979) 2.
[51] P.Y. Yu, M. Cardona, Fundamentals of Semiconductors-Physics and Materials Properties, Springer-Verlag, Berlin Heidelberg, 2001.
[52] F.-L. Kuo, Y. Li, M. Solomon, J. Du and N. D. Shepherd, J. Phys. D: Appl. Phys. 45 (2012) 065301.
[53] K. Jacobi, G. Zwicker and A. Gutmann, Surf. Sci. 141 (1984) 101.
[54] H.F. Wolf, *Semiconductors*, J. Wiley & Sons Inc. New York 1971.
[55] W. Monch, *Semiconductor Surfaces and Interfaces*, Springer-Verlag Berlin 1995.
[56] C. Maragliano, S. Lilliu, M.S. Dahlem, M. Chiesa, T. Souier, M. Stefancich, Sci. Rep. 4 (2014) 4203.
[57] S. N. Novikov and S. P. Timoshenkov , Russ. J. of Phys. Chem. A, 84 (2010) 1266.
[58] B. Pellegrini, J. Phys. D: Appl. Phys. 9 (1976) 55.
[59] H. Lüth, Surfaces and Interfaces of Solid Materials, Springer-Verlag, Berlin, 1995.
[60] B. Saha, N.S. Das, K.K. Chattopadhyay, Thin Sollid Films, 562 (2014) 37.
[61] A. Weidinger, J.M. Gil, H.V. Alberto, R.C. Vilao, J. Piroto Duarte, N. Ayres de Campos, S.FJ. Cox, Physica B,326 (2003) 124.
[62] A. Janotti and C. G. Van deWalle Phys. Rev. B 75 (2007) 165202.
[63] G. Pacchioni, ChemPhysChem, 4(2003) 1041.
[64] Polarz, Angew. Chem., Int. Ed. 45 (2006) 2965.
[65] D. Seghier, H.P. Gisalson, J. Mater. Sci: Mater Electron, 19 (2008) 687.
[66] B. Monemar, U. Lindefelt and W.M. Chen, Physica B, 146 (1987) 256.
[67] A. Janotti and C. G. Van deWalle, J. Cryst. Growth 287 (2006) 58.
[68] S.Lany and A. Zunger, Phys. Rev. Lett. 98 (2007) 045501.
[69] S.Lany and A. Zunger , Phys. Rev. B 72 (2005) 035215.
[70] A. Janotti and C. G. Van de Walle, Appl. Phys. Lett. 87 (2005) 122102.
[71] G. Pacchioni, J.M. Ricart, F. Illas, J. Am. Chem. Soc. 116 (1994) 10152.
[72] P. V. Sushko, J. L. Gavartin. A. L. Shluger, J. Phys. Chem. B 106 (2002) 2269.